Gallium defects in α-Al_2O_3: A density functional theory study

Glen R. Jenness* and Manoj K. Shukla†
Environmental Laboratory, US Army Engineer Research and Development Center, 3909 Halls Ferry Road, Vicksburg, Mississippi 39180, USA

Benjamin C. Masters
Construction Engineering Research Laboratory, US Army Engineer Research and Development Center, 2902 Newmark Drive, Champaign, Illinois 62822, USA

(Received 7 September 2023; revised 4 April 2024; accepted 14 May 2024; published 4 June 2024)

Aluminum is an important component in many consumer goods, such as automobiles. Ore refinement and the production of end products incurs a significant energy cost. An alternative is to leverage liquid metal embrittlement (LME); here, a liquid metal alloys with a solid matrix to form a brittle alloy. By outlining the desired shape, LME can produce low-cost machined parts and take advantage of recycled stock. A famous example is the LME of aluminum via gallium. An issue that arises is the formation of aluminum oxide (Al_2O_3), either as a passivation layer or along the aluminum grain boundaries. It is not clear from the existing literature how this oxide layer would impact the LME through the application of gallium. In the current study, we examine the defect formation energies of gallium in α-Al_2O_3 and its diffusion barriers as a function of gallium charge state. We find that while gallium in the +3 charge state is thermodynamically favored to insert into α-Al_2O_3, there exists a high diffusion barrier that prevents it from traveling through the Al_2O_3 matrix.

DOI: 10.1103/PhysRevB.109.235204

I. INTRODUCTION

Aluminum is a major metal that has seen extensive usage in industry [1–4], a prominent example of which is the use of aluminum parts for use in automobiles owing to its light weight, which has proven effective in the reduction of emissions and fuel usage [4,5]. This has resulted in a nearly threefold increase in aluminum usage in automobiles from 50 kg in 1990 to ∼150–180 kg in 2020 [3]. However, the standard methods of aluminum refinement from raw ore to end consumer products carries significant energy costs and requires a robust infrastructure. The prominent method of aluminum refinement is from bauxite ore [4,6–9]. In order to produce one metric ton of aluminum, five metric tons of bauxite ore is required alongside ∼10–20 gigajoules per metric ton of energy [4]. Finally, it should be mentioned that 70% of greenhouse gas emissions resulting from the aluminum production cycle originates from the smelting process alone [8]. An alternate route is to utilize recycling techniques [4,10–14]; every 1 kg of Al recycled results in 4 kg of bauxite not needing to be smelted [12]. Recycled aluminum has been proposed for usages in areas such as concrete strengthening [10], for use in mortar [13], and the production of zeolites [14]. Unfortunately, it is not only the processing of aluminum ore that is energy intensive; the manufacturing of end products is also energy intensive, whether one uses die casting [15], welding [16,17], milling [18], and/or dry turning [19].

One way to reduce the energy cost associated with the aluminum economy to manipulate the mechanical properties of aluminum through alloying it with different metals. Of particular interest is the phenomenon known as liquid metal embrittlement (LME). First appearing in 1914 [20,21], it is a technique wherein a liquid metal (e.g., mercury) is applied to a solid metal. The liquid metal then penetrates and diffuses along the grain boundaries of the solid metal, forming a brittle alloy [22–25]. While typically considered a manufacturing hazard (for example, in the welding of galvanized steel, the zinc coating becomes liquid and can diffuse into the iron matrix and lead to crack formation [26]), one can imagine a more beneficial process in which a liquid metal is used to draw a shape on a solid metal. Subsequently, a brittle alloy will form around the shape and allow for the desired end product to simply be pushed out of its matrix for further refinement. This could be utilized in the production of aluminum components by the application of gallium (Ga), which is a well-known example of LME [22,23,27–35], and is (in principal) agnostic of the aluminum source. This opens up a route to utilize recycled aluminum in a more energy-efficient method.

A problem that exists that prevents implementation is the presence of aluminum oxide. This oxide forms in two key areas: as a passivation layer on top of the exposed aluminum surface and as intergranular oxides. With regard to the passivation layer, Al_2O_3 is frequently used as a means to prevent corrosion of underlying metals [36–39]; this is due to its relatively high chemical robustness. Intergranular oxides have been shown to either hinder or help the LME process [26,40–48]; however, the impact of intergranular Al_2O_3 is not clear as there have not been many studies regarding Ga on Al_2O_3 (despite Al_2O_3 being used as a substrate for the growth

*glen.r.jenness@erdc.dren.mil
†manoj.k.shukla@usace.army.mil

of gallium nitride (GaN) [49–53] and gallium oxide (Ga_2O_3) films [54–57]). Of the few studies done on Ga with Al_2O_3, Yang *et al.* [58] found on the basis of density functional theory (DFT) that Ga binds preferentially onto $Al_2O_3(0001)$ surfaces with a binding energy of ~ -1.7 eV. Another study by Lin *et al.* [49] found using kinetics studies that Ga^{3+} adsorbs onto γ-Al_2O_3, albeit with a pH dependence.

We present a systematic exploration of the energetics involved in the addition of Ga to Al_2O_3. The focus on interstitials is owed to our interest in how Ga can interpenetrate and migrate through the α-Al_2O_3 matrix and determine if α-Al_2O_3 is an inhibitor for LME. We calculate the defect formation energy (DFE) for Ga in the zero to +3 charge states for the unoccupied Wyckoff sites of α-Al_2O_3 and find that all four sites are roughly equivalent in terms of DFE. Curiously we find for the 0 to +2 charge states the DFEs are positive but becomes negative for the +3, indicating that Ga^{3+} can form an interstitial defect in α-Al_2O_3. Upon calculation of the diffusion barriers we find that the lowest barriers exist for the zero charge state, and increases up to the +3 charge state. We attribute this phenomena to an enhanced binding between the Ga^{3+} and the surrounding atoms in the α-Al_2O_3 matrix. Overall our calculations indicate that α-Al_2O_3 would act as an inhibitor for the LME of aluminum by Ga.

II. METHODS

A. Computational methods

Our density functional theory (DFT) calculations were performed with the GPAW electronic structure package [59] with the Atomic Simulation Environment (ASE) package [60]. The projector augmented wave function (PAW) method [61–63] was used to represent the core electrons. Unit cells were initially optimized with a plane-wave basis set using a 600 eV cutoff; positions and energetics were calculated with the finite-difference basis set [61,64] with a grid spacing of 0.2 Å (such a grid spacing corresponds to a kinetic energy cutoff of ~900 eV [64]). Fermi-level discontinuities were corrected with a Fermi-Dirac smearing scheme using a smearing parameter of 0.05 eV. Energies were minimized to self-consistency using the residual minimization method-direct inversion of iterative subspace (RMM-DIIS) method [65,66] to a threshold of 10^{-6} eV. In Sec. III A we discuss our choice of exchange-correlation functional as well as our choice of k-point mesh.

The defect formation energies (DFE or E_{DFE}) are calculated in the standard fashion using the Zhang-Northrup formula [67–69]

$$E_{\mathrm{DFE}} = E_{\mathrm{defect}} - E_{\mathrm{bulk}} - \sum_{i}^{N} n_i\mu_i + q(\epsilon_{\mathrm{VBM}} + \epsilon_{\mathrm{Fermi}} + \epsilon_{\mathrm{shift}}), \tag{1}$$

where E_{defect} is the DFT energy of the defected cell and E_{bulk} is the DFT energy of the undefected cell. The $n_i\mu_i$ term denotes the dopant chemical species, with n_i being the number of atoms of dopant i and μ_i is the chemical potential of dopant i. The $q(\epsilon_{\mathrm{VBM}} + \epsilon_{\mathrm{Fermi}} + \epsilon_{\mathrm{shift}})$ term represents the chemical potential of an electron, where q is the charge of the supercell, ϵ_{VBM} is the valence band maximum, $\epsilon_{\mathrm{Fermi}}$ is the Fermi level relative to the valence band maximum (here taken to be 0), and $\epsilon_{\mathrm{shift}}$ is the core-potential shift due to the change in charge state from the neutral (note that some authors may denote this term as ΔV; however, we adopted the $\epsilon_{\mathrm{shift}}$ nomenclature as ΔV also denotes a volume change and we wish to avoid any confusion on behalf of our readers). It should be pointed out that the electron chemical potential in Eq. (1) will also need to be corrected for electrostatic interactions between defects of neighboring cells [70]. In the current study we utilized the method of Komsa and Pasquarello [71] as implemented in GPAW to get the correct for the electrostatic interactions between neighboring cells as well as providing the $\epsilon_{\mathrm{shift}}$ term.

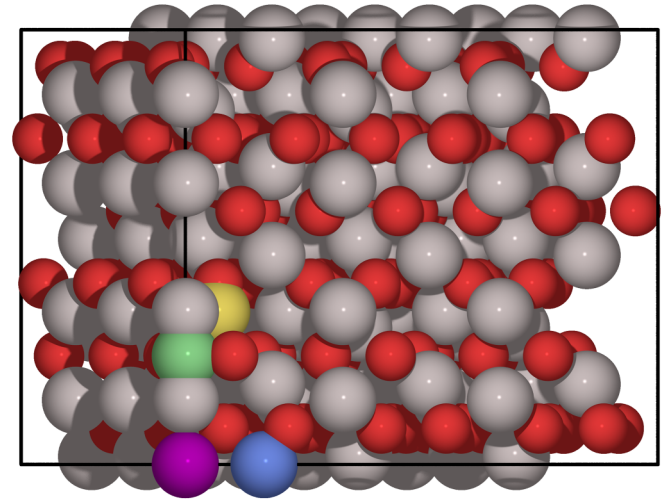

FIG. 1. Location of the various Wyckoff sites in α-Al_2O_3. Aluminum atoms (gray spheres) are located on the 12c sites and oxygen atoms (red spheres) are located at the 18e site. The green sphere denotes the 6a site, violet the 6b site, blue the 18d site, and yellow the 36f site. The solid black line denotes the unit cell boundary.

We calculate charge density differences (ρ_{diff}) according to,

$$\rho_{\mathrm{diff}} = \rho_{\mathrm{Ga^X\text{-}Al_2O_3}} - \rho_{\mathrm{Al_2O_3}} - \rho_{\mathrm{Ga^X}}, \tag{2}$$

where ρ is the all electron density from DFT, and X denotes the charge state. Atomistic charges and volumes were calculated using Bader's atoms-in-molecules [72] using the implementation of Henkelman and coworkers [73–75]. Diffusion barriers were calculated using the nudged elastic band (NEB) method [76] as implemented in ASE. Images for the NEB were optimized to a force threshold of 0.1 eV $Å^{-1}$.

B. α-Al_2O_3 structure and chemical potentials

α-Al_2O_3 belongs to the R-3c space group, which features six Wyckoff sites: 6a, 6b, 12c, 18d, 18e, and 36f. Oxygens occupy the 18e sites, and Al atoms occupy the 12c sites, resulting in the 6a, 6b, 18d, and 36f sites free for an interstitial doping of Ga. These sites are shown in Fig. 1 and their positions in crystallographic coordinates are reported in Table III. We note that for the 36f site, the coordinates depending on the position of the other atoms; in this case we were able to determine (x, y, z) from examination of the crystallographic coordinates of the aluminum and oxygen atoms (see Sec. III B 4 for more details). For the calculation of

TABLE I. Crystal structure, lattice parameters, and band gaps with respect to density functional.

Material	Crystal Structure	Functional	Lattice Parameters (Å) A	B	C	Band Gap (eV)
Gallium (Ga)	Cmce (#64)	LDA	4.450	7.480	4.459	
	A ≠ B ≠ C	PBE	4.577	7.842	4.596	
		optPBE-vdW	4.636	7.901	4.644	
		PBEsol	4.498	7.693	4.512	
		Expt [78]	4.526	7.657	4.519	
Aluminum (Al)	Fm-3m (#225)	LDA	3.989			
	A = B = C	PBE	4.045			
		optPBE-vdW	4.083			
		PBEsol	4.020			
		Expt [79]	4.040			
α-Al_2O_3	R-3c (#167)	LDA	4.709		12.811	6.633
	A = B ≠ C	PBE	4.785		13.030	6.078
		optPBE-vdW	4.788		13.033	6.240
		PBEsol	4.752		12.932	6.299
		Expt [80]	4.750		12.928	∼6.2 [81–84]

our defect formation energies, we replicated the primitive cell by $p(3 \times 3 \times 1)$ and used the Γ point for the k mesh (the rapid convergence of the α-Al_2O_3 chemical potential with respect to k-point density in Table II indicates that this is an appropriate choice).

For the solid species Ga, Al, and α-Al_2O_3 we define the chemical potential μ as,

$$\mu = \frac{E^{\mathrm{DFT}}_{\mathrm{bulk}}}{N_{\mathrm{f.u.}}}, \tag{3}$$

where $E^{\mathrm{DFT}}_{\mathrm{bulk}}$ is the DFT energy of the bulk system and $N_{\mathrm{f.u.}}$ is the number of formula units in the unit cell. For oxygen we have utilized two different chemical potentials: one originating from water and one from molecular oxygen,

$$\mu_{\mathrm{O}}(\mathrm{H_2O}) = E^{\mathrm{DFT}}_{\mathrm{H_2O}} - E^{\mathrm{DFT}}_{\mathrm{H_2}}, \tag{4a}$$

$$\mu_{\mathrm{O}}(\mathrm{O_2}) = \tfrac{1}{2} E^{\mathrm{DFT}}_{\mathrm{O_2}}, \tag{4b}$$

where E^{DFT}_{X} is the DFT energy of species X. If we take the vibrations of the molecular species in Eq. (4), we can calculate the chemical potentials as a function of temperature and pressure [77]. Here, we use the VIBRATIONS and IDEALGASTHERMO modules of ASE to calculate the thermal corrections using a temperature of 25 °C and a pressure of one atmosphere (101.325 kPa).

Certain defects and their associated chemical potentials will depend upon the conditions, i.e., whether it is oxygen or aluminum-rich. For defects involving gallium, we always assume gallium-rich conditions and therefore the chemical potential for gallium is given in Eq. (3). Under aluminum-rich conditions, we talk μ_{Al} to be defined in Eq. (3) and back calculate the oxygen chemical potential using the chemical potential of α-Al_2O_3,

$$\mu_{\mathrm{O}}(\mathrm{Al\,rich}) = \frac{\mu_{\alpha\text{-}\mathrm{Al_2O_3}} - N_{\mathrm{Al}} * \mu_{\mathrm{Al}}}{N_{\mathrm{O}}}, \tag{5}$$

where $N_{\mathrm{Al/O}}$ is the number of Al and O atoms in the α-Al_2O_3 unit cell that $\mu_{\alpha\text{-}\mathrm{Al_2O_3}}$ is calculated from. In a similar fashion, under oxygen-rich conditions μ_{O} is calculated according to Eq. (4) and μ_{Al} is calculated from α-Al_2O_3,

$$\mu_{\mathrm{Al}}(\mathrm{O\,rich}) = \frac{\mu_{\alpha\text{-}\mathrm{Al_2O_3}} - N_{\mathrm{O}} * \mu_{\mathrm{O}}}{N_{\mathrm{Al}}}, \tag{6}$$

where μ_{O} is from either Eqs. (4a) or (4b).

III. RESULTS AND DISCUSSION

A. Choice of functional and k points

In order to determine the best functional and choice of k points, we examined the unit cell parameters for bulk Ga, Al, and α-Al_2O_3 to experimental values in Table I. The choice of the α form of Al_2O_3 is mediated by the fact that this is the lowest-energy polymorph [85,86] and has been found to exist as an intergranular oxide [41]. For the calculations of our lattice parameters, we initially utilized a k-point mesh of $3 \times 3 \times 3$ as this grid has served us well in prior studies [87–91] for the calculation of unit cell parameters. We examined the LDA [92], PBE [93], optPBE-vdW [94,95], and PBEsol [96] functionals. Gallium (Ga) belongs to space group Cmce (#64) where (where A ≠ B ≠ C). Barnett and Spooner reported lattice constants of [A, B, C] = [4.526, 7.526, 4.519]Å; optPBE-vdW overestimates these parameters by ∼0.15 Å. Conversely, LDA underestimates these values by roughly the same amount. PBE does the best, with PBEsol close behind it. For aluminum (Al), the space group is cubic (Fm-3m, #225) and thus there is only one lattice parameter to determine. Similar for Ga, optPBE-vdW and LDA both over- and underestimate the lattice constant (respectively). PBE and PBEsol are fairly close to each other, with PBE edging out PBEsol. Finally for α-Al_2O_3 (space group R-3c, #167) we find once again optPBE-vdW and LDA over- and underestimates (respectively) the two lattice constants (A and C). However, we find that PBE also overestimates the lattice constants and are nearly identical to the optPBE-vdW results.

TABLE II. Optimal k-point density and meshes, and chemical potentials [with chemical potentials defined in Eq. (3)].

Material	k density	k mesh	Chemical potential (eV)
Gallium (Ga)	3.00	$5 \times 3 \times 5$	–3.34
Aluminum (Al)	4.00	$7 \times 7 \times 7$	–4.09
α-Al_2O_3	2.00	$3 \times 3 \times 1$	–40.71

In addition to calculating the lattice constants, we also considered how the band gap differs with choice of functional. We report our results in Table I. As gallium and aluminum are referenced to their metallic states we do not consider their band gap as it is zero by definition. Experimentally the band gap of α-Al_2O_3 has been determined to be ∼6.2 eV [81–84]; LDA overestimates this value by ∼0.4 eV. Conversely PBE, optPBE-vdW, and PBEsol are closer with differences of ∼0.2 eV, ∼0.04 eV, and ∼0.1 eV, respectively. Given that PBEsol does the best for capturing the experimental lattice constants of α-Al_2O_3 and the small error this functional has in the calculation of the band gap, we will be using PBEsol for the remainder of our study.

Having established PBEsol as our density functional of choice, we now turn to our choice of k-point mesh. This choice is of particular concern for our chemical potentials as energetics are more slow to converge with respect to k points than geometrical parameters. In Fig. S1 of the Supplemental Material [97] we plot the energy of a formula unit for three bulk crystals of Ga, Al, and α-Al_2O_3 for a Γ-centered k-point mesh. In order to make the plots easier, we plot the chemical potential as a function of the k-point density, which is defined as,

$$\rho_{\mathbf{k}} = \mathbf{N}\frac{\mathbf{a}}{2\pi}, \tag{7}$$

where $\mathbf{N}$ is a vector specifying the number of k points and $\mathbf{a}$ denotes the lattice vector. For Ga we find the k points are converged at a $\rho_{\mathbf{k}}$ of 3, for Al it is converged at 4, and for α-Al_2O_3 it is converged at 2 [97]. Converged k-point densities, the associated k-point mesh, and μ_i's are reported in Table II.

B. Ga defects in α-Al_2O_3

1. Ga@6a

In terms of crystal coordinates, the 6a Wyckoff site is located at $(0,\ 0,\ \frac{1}{4})$. Insertion of the Ga at this location and its resulting location following optimization is shown in Fig. 2. Upon optimization of the unit cell, the Ga defect pushes onto the neighboring Al^{3+} atoms, resulting in one Al^{3+} species to partially occupy the 6b Wyckoff site. From Table III the addition of a metallic Ga^0 species is an endothermic process, with a DFE of 10.6 eV. Removal of an electron lowers the DFE to 5.4 eV. Removal of a second electron further lowers the DFE to 2.4 eV, and finally the Ga^{3+} state is exothermic with a DFE of −1.2 eV. Compared to the undefected α-Al_2O_3 crystal, the 6a defect expands the volume of the unit cell slightly by 1.2%. The degree of volumetric expansion is also very slight for the +1 and +2 states; however for the +3 state we see a contraction of the unit cell volume compared to the pristine (i.e., undefected) crystal cell.

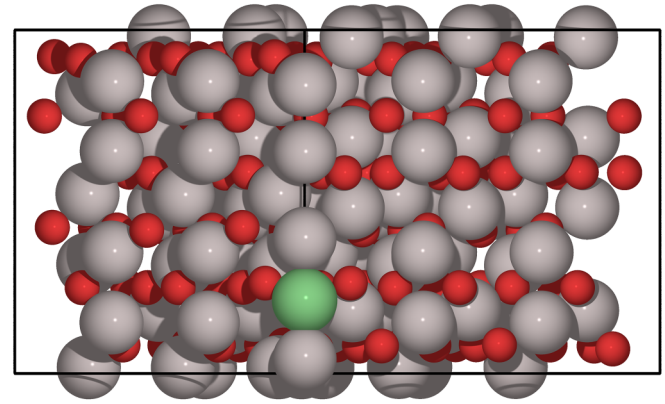

FIG. 2. Optimized Ga defect at the 6a Wyckoff site. Red, gray, and green spheres denote oxygen, aluminum, and gallium, respectively. The solid black line denotes the unit cell boundary.

In Table S1 [97], we report the Ga nearest-neighbor distances up to ∼3 Å with the atomic charges and volumes from a Bader charge density analysis [97]. For charge states 1–3, we report the changes in these values relative to the neutral defect; if the value is negative it has decreased, while a positive value denotes that it has increased. In terms of atomic charges, this means that if Δq is negative then that atom has gained electrons and vice versa. For the Ga@6a, we find that there are three O^{2-} at ∼2 Å, two Al^{3+} at ∼2.2–2.3 Å, three O^{2-} at 2.6 Å, and finally three Al^{3+} at 2.8 Å. With the exception of the Al^{3+} at 2.2 and 2.3 Å, all the nearest neighbors are relatively consistent in terms of charges and volumes. The exceptions are the Al^{3+} species that are on either side of the Ga in the z direction as shown in Fig. 2 [these Al^{3+} sites are marked with an asterisk (*) in Table S1] [97]. The charges for these two species are lower than the other Al^{3+}

TABLE III. Interstitial Ga defects in α-Al_2O_3 with different reference states as a function of Ga charge.

Wyckoff Position	Charge	% ΔV (Å^3)	Defect Formation Energy (eV) Metallic	$Ga(OH)_3$	$Ga(NO_3)_3$
6a	0	1.22%	10.64		
$(0,\ 0,\ \frac{1}{4})$	1	0.59%	5.39		
	2	0.16%	2.40		
	3	−0.31%	−1.17	−1.95	−3.49
6b	0	0.99%	9.92		
(0, 0, 0)	1	0.48%	5.82		
	2	0.07%	2.64		
	3	−0.34%	−1.04	−1.82	−3.36
18d	0	0.89%	10.75		
$(\frac{1}{2},\ 0,\ 0)$	1	0.52%	5.38		
	2	0.07%	2.63		
	3	−0.34%	−1.06	−1.84	−3.38
36f	0	0.85%	10.77		
$(x,\ y,\ z)$	1	0.53%	5.32		
	2	0.09%	2.50		
	3	−0.34%	−1.12	−1.90	−3.44

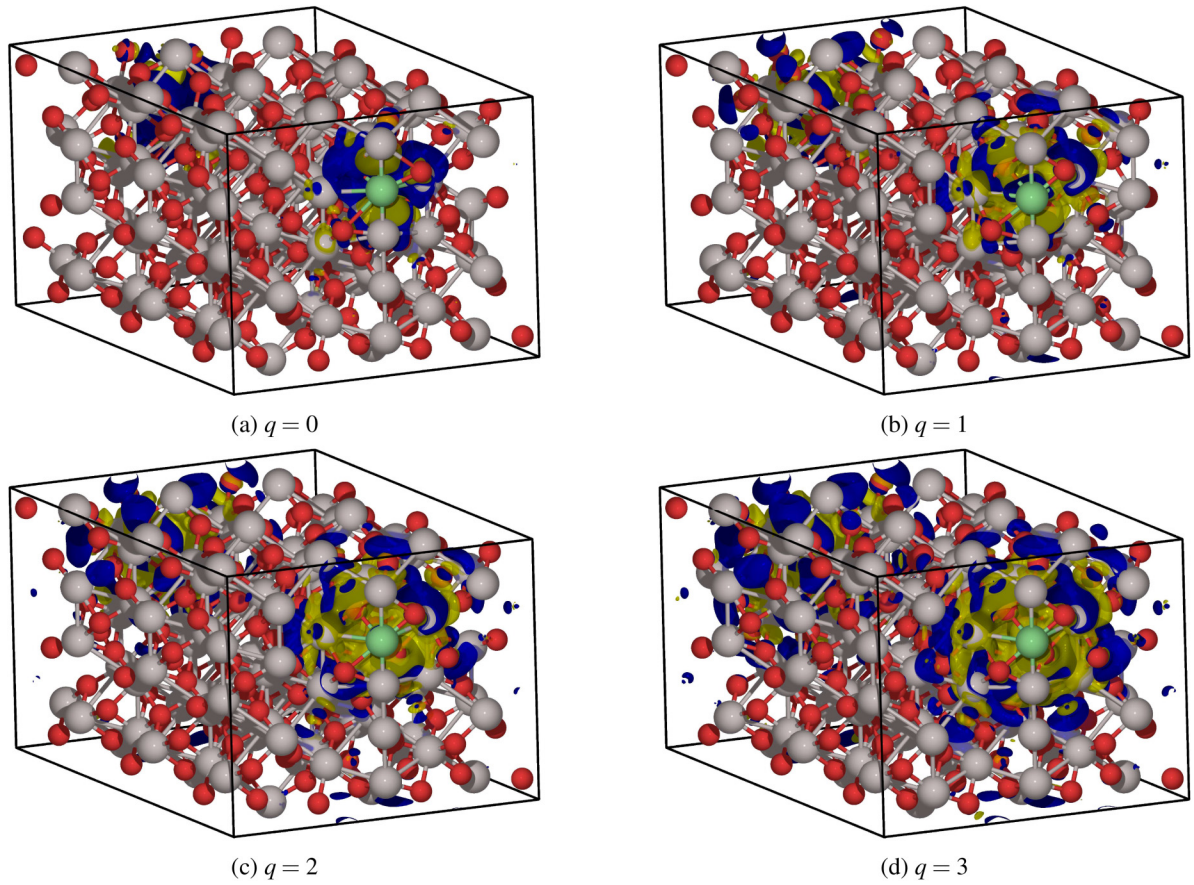

FIG. 3. Charge density differences for a Ga interstitial at the 6a Wyckoff site for charge states 0–3. Red, gray, and green spheres denote oxygen, aluminum, and gallium, respectively. The solid black line denotes the unit cell boundary. The atoms and density grid were shifted by 0.5 of the unit cell in the x and z direction for ease of visualization around the periodic boundaries. Isosurface shown is the 1×10^{-3} e^- Å^{-3}. Yellow regions denotes areas of charge accumulation whereas blue denotes areas of charge depletion.

species; however, it should be noted that the neighboring Ga also has a small partial charge of ∼0.3 e^-. This demonstrates that as we add in the Ga, it forms a small positive charge state by donating electron density to the Al^{3+} species that is has displaced in forming the defect. This picture is further supported when we examine the atomic volumes; here we see an increase in volume that is consistent with the donation of electron density from a neighboring atom.

As we increase the charge state, we find that the Ga accumulates a more positive charge and a decrease in the atomic volume; for the +3 state the atomic volume has decreased by ∼50%. The atomic volumes of the neighboring oxygens changes very little; this is in line with the negligible differences in atomic charges for these species. The nearest Al^{3+} species show a slight loss of electrons with a contraction of the atomic volumes. This is in line with the charge state being delocalized; however, this delocalization is still centered around the Ga defect. These changes and the delocalization effect can be visually seen from the charge density differences shown in Fig. 3. From this figure we can see that as we move from the neutral to a higher charge state, the positive region grows and creates a roughly spherical region of negative charge. Moreover we also observe that the interatomic distances also decrease, with the degree of decreasing being related to an increase in the charge state. Table S1 also demonstrates the origin of the volume contractions reported in Table III, i.e., namely that the introduction of a positive charge state causes not only a contraction of the atomic volumes, but also the atomic bonds in α-Al_2O_3 [97].

2. Ga@6b

The crystal coordinate of the 6b Wyckoff site is located at the origin of the unit cell. Optimization of this defect is shown in Fig. 4. In contrast to the 6a site, the defect at the 6b site does not cause a major displacement of neighboring atoms. Examination of the nearest neighbors shows two Al^{3+} sites at 2.21 Å, six O^{2-} sites also at 2.25 Å, and six Al^{3+} sites at 2.87 Å. In the neutral crystal, the Ga carries a small positive charge of 0.13 e^-, the nearest Al^{3+} sites carries a charge of 2.37 e^-, the oxygens –1.65 e^-, and the far aluminums 2.52 e^-. In terms of nearest-neighbor interactions, the 6b defect does not introduce the type of polarization shown for the 6a site, i.e., the atomic charges and volumes of the neighbors are consistent with each other. Moving to a higher charge state we observe an accumulation of positive charge on the Ga atom and a decrease in the atomic volume; these changes are in line with what we reported for the 6a defect above. In contrast to the 6a defect, for the 6b defect the atomic volumes for two of the oxygens are much smaller than the other four. This

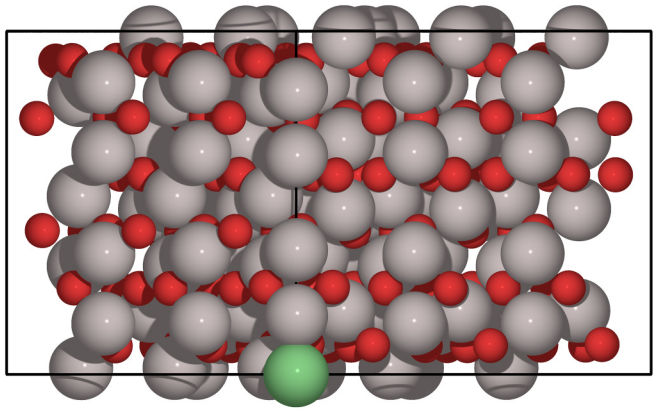

FIG. 4. Optimized Ga defect at the 6b Wyckoff site. Red, gray, and green spheres denote oxygen, aluminum, and gallium, respectively. The solid black line denotes the unit cell boundary.

contraction starts at the +1 charge state, and is amplified as we move towards the +3. These two oxygen atoms also lose electron density, and become less negative than their fellow oxygen atoms. Moreover these two oxygen atoms experience a slight elongation of their chemical bonds with a higher decrease in their atomic volumes in contrast to their fellows. For the nearest Al^{3+} sites, there is a loss of electron density leading to a higher atomic charge and a contraction of atomic volumes. For the far Al^{3+} sites, these are relatively unchanged from the neutral crystal [97]. In terms of the DFE energetics, the 6b site follows the same trends that we saw for the 6a; namely, the neutral crystal has a high DFE of ∼10 eV, which decreases to –1.12 eV for the +3 charge state.

3. Ga@18d

The 18d Wyckoff site is located at $(\frac{1}{2}, 0, 0)$ and its resulting location following optimization is shown in Fig. 5 . While insertion of Ga at the 18d site does not cause a dramatic shift in the surrounding atomic positions like we observed with the 6a site, there are still significant changes in the local environment, which is in contrast with what we observed with the 6b site. From Table S3 [97], we can see

TABLE IV. Site locations for the 12c and 18e Wyckoff sites of spacegroup R-3c (#167). Taken from the database of Aroyo *et al.* [98][a].

Site	Crystal Coordinates	
12c	$(0, 0, z)$	$(0, 0, -z+\frac{1}{2})$
	$(0, 0, -z)$	$(0, 0, z+\frac{1}{2})$
18e	$(x, 0, \frac{1}{4})$	$(0, x, \frac{1}{4})$
	$(-x, -x, \frac{1}{4})$	$(-x, 0, \frac{3}{4})$
	$(0, -x, \frac{3}{4})$	$(x, x, \frac{3}{4})$

[a]Located online [102].

that gallium's nearest neighbors are two O^{2-}; while the two different Ga-O bond lengths may suggest a polarization of these bonds upon optimization, the equality in the atomic charges suggests otherwise. However, the atomic volumes of these two oxygens do differ by 0.60 $Å^3$. As we increase the crystal charge, we observe a similar trend to the 6a and 6b sites, *i.e.* there is a growing positive charge on the Ga, a contraction in gallium's atomic volume, and a contraction of the intercrystal bonds. The positive charge is localized around the Ga, and has an increasing diffusivity as the charge state increases (see Fig. S3 [97]). The DFE energetics are similar to what have been discussed above for the 6a and 6b sites.

4. Ga@36f

Unlike the three previous Wyckoff sites, the 36f Wyckoff site is located at (x, y, z) where the xyz are defined by examining the crystal coordinates of the other atoms in the cell. Using the symmetry information given by Aroyo *et al.* [98], we can determine the z coordinate by considering the crystal coordinates of the 12c aluminum sites and we can determine the xy by looking at the 18e oxygen sites. The crystal coordinates for both sites are given in Table IV. This gives us the location of the 36f site as (0.3, 0.3, 0.35). Insertion of the Ga at this location and its resulting location following optimization is shown in Fig. 6.

Optimization of the Ga position results in a shift in the crystal coordinates; however, we do not observe any major rearrangements in the α-Al_2O_3 crystal. Similar to what has been

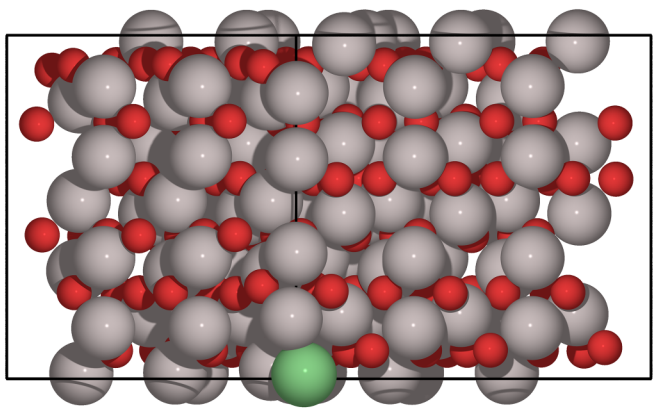

FIG. 5. Optimized Ga defect at the 18d Wyckoff site. Red, gray, and green spheres denote oxygen, aluminum, and gallium, respectively. The solid black line denotes the unit cell boundary.

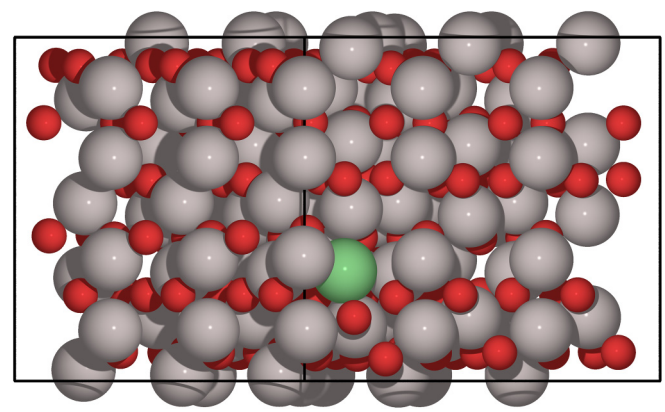

FIG. 6. Optimized Ga defect at the 36f Wyckoff site. Red, gray, and green spheres denote oxygen, aluminum, and gallium, respectively. The solid black line denotes the unit cell boundary.

TABLE V. Ga substitution defects in α-Al_2O_3 as a function of charge.

Defect	Charge	% ΔV (Å^3)	DFE (eV) Al Rich	DFE (eV) O Rich[a]
Ga@Al Substitution	0	0.13%	2.89	−1.33 / −4.69
	1	−0.16%	3.45	−0.77 / −4.13
	2	−0.48%	4.39	0.17 / −3.19
	3	−0.78%	5.59	1.37 / −1.98
Ga@O Substitution	0	0.84%	8.41	11.23 / 13.47
	1	0.39%	4.73	7.55 / 9.78
	2	−0.02%	1.82	4.64 / 6.87
	3	−0.41%	−1.07	1.75 / 3.98

[a]The DFE to the right of the slash denotes a reference state of water and to the left of the slash a reference state for molecular oxygen (O_2).

discussed above, the DFE of the neutral crystal is ∼10 eV, and decreases to ∼–1 eV for the +3 charge state. Moreover, we further observe similar changes in the atomic volume of the Ga (which is in line with the removal of electrons) with a contraction of the Ga-Al and Ga-O bonds. The positive charge is largely focused around the Ga, and becomes more diffuse as the charge state increases (see Fig. S4 [97]).

5. Ga substitutions

In addition to the interstitial sites mentioned above, we can also introduce a Ga defect into α-Al_2O_3 as a substitutional defect wherein either an Al or O atom is replaced with a Ga. We report the DFEs for such a defect in Table V for $0 \leqslant \delta q \leqslant +3$ and show the optimized structure in Fig. 7. As we are removing atoms from the α-Al_2O_3 matrix, we need to consider the DFEs as a function of the chemical potential of these native atoms as shown in Eqs. (3) and (4). From our results, we can see that Ga replacing an oxygen atom under Al-rich conditions is a fairly endothermic process with a positive DFE; however, in contrast to the results for the interstitials where the DFE got more favorable as Δq changes from 0 to +3, the DFE for a Ga substitution becomes more unfavorable (i.e., becomes more positive) as we increase Δq. This is a trend that continues under oxygen-rich conditions; however, here the DFE starts off favorable (–1.3 eV and –4.7 eV for water and O_2 reference, respectively), and trends upwards as we increase Δq. We find that for Ga_3^+ a water reference results in a positive DFE, whereas for an O_2 reference the DFE is still negative.

For a Ga substitution at an Al site we find a similar trend in the DFE's with respect to charge that we observed for the interstitials. Under Al-rich conditions, the DFE starts at 8.4 eV for $\Delta q = 0$ and trends downwards and becomes –1.1 eV at $\Delta q = +3$. Under oxygen-rich conditions the DFE starts at 11.2 eV and 13.5 eV and decreases to 1.8 eV and 4.0 eV (for water and O_2 reference, respectively).

6. Molecular Ga reference

In the above calculations, we observed that the Ga^{3+} defect has a negative DFE, indicating that it is an exothermic process for the addition of Ga^{3+} into α-Al_2O_3. In order to probe this further we considered a reference coming from two molecular species: gallium hydroxide [$Ga(OH)_3$] and gallium nitrate [$Ga(NO_3)_3$]. We used the following chemical reactions for our reference,

$$Ga(OH)_3 + 3H_3O^+ \rightleftharpoons Ga^{3+} + 6H_2O \quad (8a)$$

$$Ga(NO_3)_3 + 3H_3O^+ \rightleftharpoons Ga^{3+} + 3H_2O + 3HNO_3. \quad (8b)$$

By assuming equilibrium, we can do a simple rearrangement of Eq. (8) to solve for the energy of Ga^{3+} and insert that into Eq. (1). As this is a demonstrative exploration, we did not consider the effect of solvent in Eq. (8), i.e., all species were in the gas phase. The resulting DFE's with these references are reported in Table III. From here we can see that the $Ga(OH)_3$ reference lowers the DFE's by a further 1 eV, indicating a more exothermic process. This effect is further enhanced when considering the $Ga(NO_3)_3$ reference with DFE's ranging from ∼–3.3 eV to ∼–3.5 eV. These calculations indicate that there is a possible chemical treatment

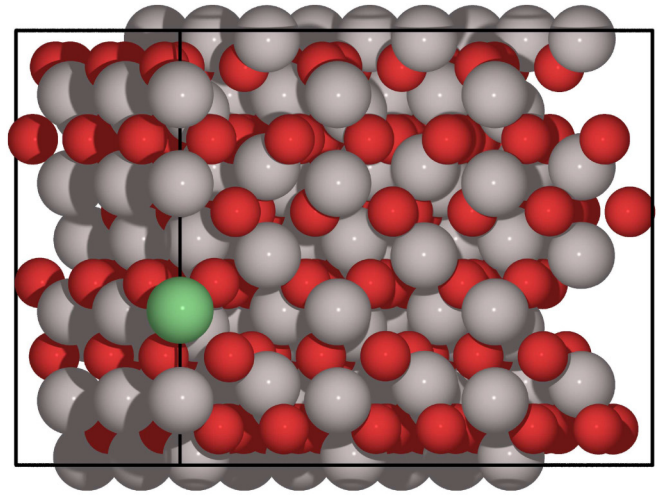

(a) Ga@Al

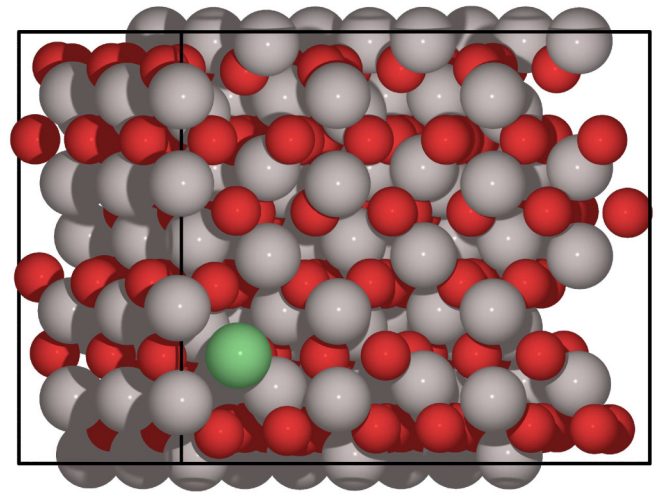

(b) Ga@O

FIG. 7. Optimized substitutional Ga defects. Red, gray, and green spheres denote oxygen, aluminum, and gallium, respectively. The solid black line denotes the unit cell boundary.

TABLE VI. Al interstitial defects in α-Al_2O_3 with different reference states as a function of defect charge.

Wyckoff		% ΔV	DFE (eV)	
Position	Charge	(Å^3)	Al Rich	O Rich[a]
6a	0	1.22%	9.59	13.81 / 17.17
(0, 0, $\frac{1}{4}$)	1	0.67%	5.33	9.55 / 12.91
	2	0.26%	0.64	4.87 / 8.22
	3	−0.30%	−3.85	0.38 / 3.73
6b	0	1.07%	9.99	14.21 / 17.57
(0, 0, 0)	1	0.76%	4.55	8.78 / 12.13
	2	0.15%	−0.06	4.17 / 7.52
	3	−0.48%	−4.41	−0.19 / 3.16
18d	0	1.37%	23.96	28.18 / 31.54
($\frac{1}{2}$, 0, 0)	1	0.52%	4.29	8.51 / 11.86
	2	0.14%	−0.10	4.12 / 7.48
	3	−0.48%	−4.45	−0.22 / 3.13
36f	0	1.19%	9.79	14.01 / 7.36
(x, y, z)	1	0.55%	5.06	9.28 / 12.64
	2	0.14%	−0.26	3.96 / 7.31
	3	−0.48%	−4.75	−0.53 / 2.83

[a]The DFE to the right of the slash denotes a reference state of water and to the left of the slash a reference state for molecular oxygen (O_2).

for the insertion of Ga into α-Al_2O_3 and would be worthy of a further investigation.

C. Intrinsic defects in α-Al_2O_3

Before presenting a further analysis of the effect of gallium doping in α-Al_2O_3, it is instructive to consider intrinsic (i.e., native) defects in α-Al_2O_3. In the current study we consider the effect of interstitials (defects located at spaces between atoms), vacancies (the removal of an atom), and antisites (where one atom of the parent matrix replaces another). Results are located in Tables VI–VIII.

TABLE VII. Oxygen interstitial defects in α-Al_2O_3 with different reference states as a function of defect charge.

Wyckoff		% ΔV	DFE (eV)	
Position	Charge	(Å^3)	Al Rich	O Rich[a]
6a	−2	1.58%	30.63	27.82 / 25.58
(0, 0, $\frac{1}{4}$)	−1	0.67%	14.09	11.27 / 9.04
	0	0.26%	11.92	9.10 / 6.87
6b	−2	1.05%	13.96	11.14 / 8.91
(0, 0, 0)	−1	0.64%	11.73	8.92 / 6.68
	0	0.28%	10.61	7.79 / 5.55
18d	−2	1.00%	12.87	10.06 / 7.82
($\frac{1}{2}$, 0, 0)	−1	0.98%	13.17	10.36 / 8.12
	0	0.54%	9.80	7.98 / 4.75
36f	−2	1.00%	12.99	10.17 / 7.94
(x, y, z)	−1	0.59%	11.29	8.48 / 6.24
	0	0.27%	8.30	5.48 / 3.25

[a]The DFE to the right of the slash denotes a reference state of water and to the left of the slash a reference state for molecular oxygen (O_2).

TABLE VIII. Intrinsic vacancy and antisite defects in α-Al_2O_3 as a function of charge.

		% ΔV	DFE (eV)	
Defect	Charge	(Å^3)	Al Rich	O Rich[a]
Al Vacancy	−3	1.12%	12.49	8.27 / 4.91
	−2	0.70%	12.21	7.99 / 4.63
	−1	0.40%	12.19	7.97 / 4.61
	0	0.08%	12.60	8.38 / 5.02
O Vacancy	0	−0.08%	1.87	4.68 / 6.92
	1	−0.31%	−0.18	2.64 / 4.87
	2	−0.53%	−2.40	0.41 / 2.65
Al@O Antisite	−1	1.38%	21.80	28.84 / 34.43
	0	0.87%	21.82	28.86 / 34.45
	1	0.37%	22.12	29.16 / 35.75
	2	−0.08%	22.89	29.93 / 35.52
	3	−0.53%	23.91	30.95 / 36.54
O@Al Antisite	−1	0.41%	21.57	18.76 / 16.52
	0	0.09%	21.76	18.94 / 16.71
	1	−0.24%	21.79	18.98 / 16.74
	2	−0.59%	21.44	18.62 / 16.38
	3	−0.89%	20.70	17.88 / 15.65

[a]The DFE to the right of the slash denotes a reference state of water and to the left of the slash a reference state for molecular oxygen (O_2).

1. α-Al_2O_3 *interstitials*

We first examine Al interstitials (with results given in Table VI), starting with the 6a Wyckoff site. Initial placement of an Al atom at this location results in nearest-neighbor aluminum interactions that are too close; upon optimization the repulsive forces arising from the small Al-Al distance results in the neighboring Al atoms being displaced. Under Al-rich conditions, a neutral Al defect has a DFE of 9.6 eV; as we increase the charge on this defect the DFE becomes more negative and thus exothermic and more favorable. Moreover an increase in the charge state results in a slight contraction of the unit cell; however, the changes in the unit cell volume are fairly negligible. Moving to the 6b and 18d Wyckoff sites we find a similar pattern in the DFE's; however addition of Al to the 6b position is slightly more energetically favorable for the charged species than it is for the 6a site. We also note an exception in the trend for the Al^0 state for the 18d position; here the DFE is 24 eV, which is over twice the similar value for the other three Wyckoff sites. No explanation is forthcoming for this difference as several attempts have been tried to reoptimize this structure and calculate its energy. Lending further credence that this DFE is physical is that the charge states for the 18d are in line with what we observe for the 6a, 6b, and 36f sites; these charge states were calculated using the neutral as a starting structure and therefore if there was a problem with the structure, then these energies would also be anomalous. Therefore we are forced to conclude that this DFE is in fact physical. We do note that the 18d unit cell for the zero charge state does expand more than what we have shown for the other sites, which does offer some explanation for the high DFE of this Wyckoff position. Addition of an Al at this site follows the

trend established above; at neutral charge the DFE is ∼10 eV, and decreases to –4.75 eV at the +3 state.

For all four Al interstitials, changing the origin of μ_{Al} from Al-rich conditions to oxygen-rich conditions results in the DFE becoming more positive. Under these conditions, we do not observe a charge state of Al in which the addition of an interstitial defect is thermodynamically favorable (it is worth mentioning that under a water reference the +3 charge state is nearly thermoneutral).

We next consider the effect of adding an oxygen atom into the interstitial Wyckoff positions with our results shown in Table VII. For the 6b, 18d, and 36f sites varying the charge from –2 to 0 results in the DFE changing from 12–14 eV to 8–11 eV under aluminum-rich conditions. These values decrease under the two oxygen-rich conditions we consider, with the O_2 reference having the lower DFEs. In contrast to the Al interstitials in Table VI we do not observe any oxygen interstitial charge states with a thermodynamically favored DFE as the lowest DFE for an oxygen interstitial is 3.25 eV (compared to –4.75 eV for Al interstitials). The 6a site, however, does not follow the trend shown by the other three sites as it starts at a DFE of 31 eV for a –2 oxygen charge and going to 12 eV for neutral under Al-rich conditions. We attribute this increase in the DFE to the additional swelling caused by the defect.

2. α-Al_2O_3 *vacancies and antisites*

Finally we consider the creation of vacancy and antisite defects in α-Al_2O_3 and report our results in Table VIII. Removal of an Al atom would create a negatively charged hole; however for all charge states considered here the DFE is ∼12 eV under Al-rich conditions. Under oxygen-rich conditions, the DFE lowers to 8.4 and 5.0 eV for a water and O_2 reference, respectively. For an oxygen vacancy and the associated formation of a positively charged hole the DFE is favorable with a value of –2.4 eV for a $\Delta q = +2e^-$. Conversely, removing an oxygen under O-rich conditions results in a more positive DFE than we observed under Al-rich conditions. For antisites we find relatively large DFEs that are above +15 eV regardless of type, charge, and chemical potential reference.

D. Analysis of defect concentrations

Having examined the effect of Ga defects in α-Al_2O_3 and the intrinsic defects of α-Al_2O_3, we turn our attention to examining the effect of the DFEs on defect concentrations. Following Jacobs *et al.* [99], we can write the concentration of a defect as

$$[\text{Defect}_i] = \rho_N^i \times \exp\left(-\frac{E^i_{\text{DFE}}}{k_B T}\right), \tag{9}$$

where ρ_N^i is a number density representing the number of sites for defect i per unit cell volume, k_B is Boltzmann's constant, and T is the temperature (here taken to be at 25 °C). As the DFE is dependent upon the choice of Fermi level [see Eq. (1)], then it follows that the defect concentration in Eq. (9) is also dependent upon that choice. At this point, one can construct a charge balance equation wherein all the concentration of negative charged defects (plus the concentration of electrons) are set equal to the concentration of the positive charged defects (plus the electron hole concentration) and then determine where the Fermi level lies in the presence of the defects [99–101]. For the following analysis we will only consider oxygen-rich conditions as the introduction of Ga to a α-Al_2O_3 matrix typically occurs under atmospheric conditions with no aluminum sink present.

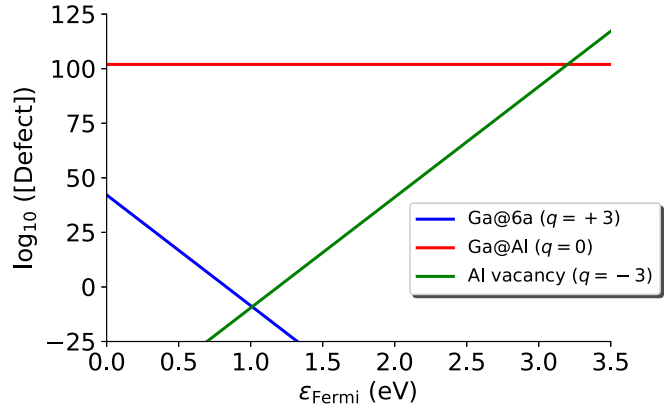

FIG. 8. Log plot of defect concentration for the Ga@6a interstitial compared to the concentration of the Ga@Al substitution under oxygen-rich conditions with an O_2 reference as a function of Fermi level. Concentrations are calculated according to Eq. (9).

From Eq. (9), we can immediately discard any defects that have a high (and positive) DFE; this leaves us with two types of defects that have a negative DFE: Ga^{+3} interstitials and Ga@Al substitutions with an O_2 reference. In lieu of the traditional Brouwer diagram (wherein one plots DFE vs. ϵ_{Fermi}), we plot the log of the concentrations (with concentrations in cm^{-3}) versus the Fermi level in Fig. 8. From here we can see that a neutral Ga@Al defect would have the largest concentration; as it is a neutral species, its concentration is independent of the choice of Fermi level. Conversely the interstitial Al^{+3} defect starts off as several orders of magnitude less than the Ga@Al defect, and trends downwards as we increase the Fermi level. While these results seem to indicate that the dominate defect would then be the Ga@Al close to the conduction band maximum (CBM), there is a nuance that we have to consider; namely that a substitutional defect is comprised of the following set of chemical reactions:

$$\alpha\text{-}Al_2O_3 + 3e^- \longrightarrow \alpha\text{-}Al_{2-x}O_3^{-3} + Al_x \tag{10a}$$

$$\alpha\text{-}Al_{2-x}O_3^{-3} + Ga_x \longrightarrow \alpha\text{-}Al_{2-x}O_3Ga_x, \tag{10b}$$

where the species α-$Al_{2-x}O_3^{-3}$ denotes an α-Al_2O_3 crystal with a Ga vacancy carrying a –3 charge. The DFE for such a vacancy is 4.9 eV. From Fig. 8 this defect has a negligible concentration at the CBM with it being equal in concentration to the Ga@Al defect at a Fermi level of ∼3.2 eV. Therefore we conclude that while Ga@Al has a more favorable DFE than the interstitial Ga defects, the important defects to consider near the CBM are the Ga interstitials (with the caveat that we are discussing a charge state of +3).

E. Diffusion of Ga in the α-Al_2O_3 crystal

From the above results, as we increase the charge state on the Ga defect we have more a favorable defect formation

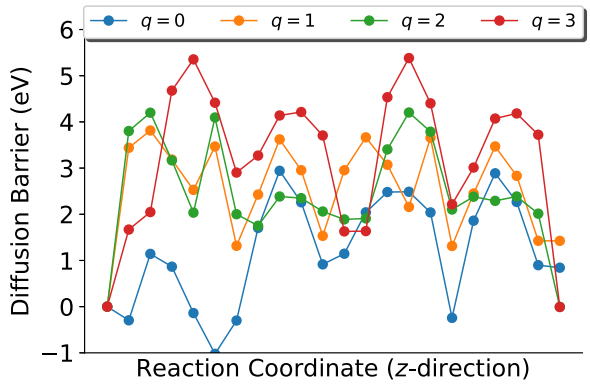

FIG. 9. Reaction pathway for the diffusion of Ga as a function of charge state in the z direction.

energy. The next question we want to answer is how readily can Ga in its various charge states migrate through the α-Al_2O_3 lattice. To answer this question we performed a series of nudged elastic band (NEB) calculations as outlined in Sec. II. We limit our discussion here to diffusion starting from the 6a Wyckoff site as this has the lowest defect formation energies; however, as the other sites are close in energy we expect that the results for the 6a site are transferable to the other three sites.

We first examined the migration of Ga in the $+z$ direction, where diffusion of Ga is mediated via a series of hops over adjacent Al atoms. The resulting energy pathways for the 0, $+1$, $+2$, and $+3$ charge states are shown in Fig. 9. For the neutral crystal the initial migration of Ga is low barrier at $\sim$1 eV; however as we move through the $+z$ direction the barrier increases to a maximum of 2.94 eV. The overall reaction pathway gets more energetically disfavored as we increase the charge state, resulting in barriers of 3.81 eV, 4.20 eV, and 5.38 eV for the $+1$, $+2$, and $+3$ charge states, respectively. The origin of this increase in barrier can be readily explained by examination of the unit cell volume contractions reported in Table III, and the contractions in bond lengths from Table S1 [97]. Essentially, we observe an overall contraction of bond lengths, which result in a contraction of the unit cell; this indicates that as we increase the Ga defect charge state we are creating a more positive bonding environment and an increase in the Ga-Al and Ga-O bond strengths results in a harder to migrate Ga defect.

For diffusion in the x and y directions we only consider the neutral crystal and the $+3$ charge state with our results shown in Fig. 10. Diffusion in the x and y directions is mediated via a series of moves through Al-O bonds and displacement of the oxygen atoms. For the x direction, the diffusion barriers for the neutral and $+3$ states are 4.29 eV and 6.83 eV, respectively; for the y direction these barriers are 4.12 eV and 5.19 eV. As we are actively breaking Al–O bonds in these directions (as opposed to the z direction where the Al atoms still kept their oxygen bonds), the higher diffusion barriers are to be expected. The exception is for the $+3$ state in the y direction; this diffusion barrier is lower than its analog in the z direction by $\sim$0.2 eV. The origin of this slight lowering is unknown; however, the high diffusion barriers reported here indicate that regardless of direction or charge state, migration of Ga through the α-Al_2O_3 crystal is kinetically prohibited.

IV. CONCLUSIONS

In the current study we examined the defect formation energies of Ga insertion into the interstitial vacancies of α-Al_2O_3. We began our study by examining which density functional would be the best for studying α-Al_2O_3. After considering the functionals LDA, PBE, PBEsol, optPBE-vdW we found that the PBEsol functional gave the most consistent results. Following this we examined the crystal structure of α-Al_2O_3 and found four possible Wyckoff sites for forming an interstitial Ga defect: the 6a, 6b, 18d, and 36f. Insertion of a Ga at each site and varying the charge state from 0–3 was carried out and defect formation energies were calculated. For each site, the DFE's start at $\sim$10 eV for a neutral crystal, and decrease to $\sim$–1 eV for the $+3$ charge state. Increasing the charge results in a contraction of the unit cell, which is due to a contraction of the Ga-Al and Ga-O bonds as well as the atomic volumes of Ga and its nearest neighbors. We also find that the positive charge is largely localized around the interstitial Ga, but becomes more diffuse as we increase the charge state. Changing the Ga reference from a metallic source to one from $Ga(OH)_3$ or $Ga(NO_3)_3$ results in a further decrease in the DFE for the $+3$ charge state, indicating a possible route for further chemical treatment.

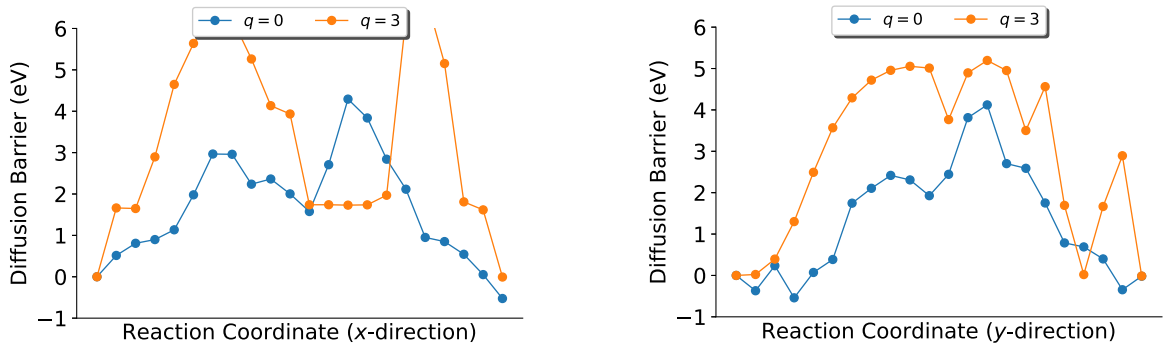

(a) x-direction (b) y-direction

FIG. 10. Reaction pathway for the diffusion of Ga for the neutral crystal and the $+3$ charge state in the x and y directions.

We next calculated the diffusion barriers for Ga at the 6a site in the three cardinal directions. We find that for the z direction diffusion is mediated by a series of Ga-Al hops. For the neutral crystal the diffusion barrier is ∼3 eV, and increases to ∼5.3 eV as we increase the charge state. A similar trend is observed for the x and y directions. This increase in the diffusion barrier is attributed to an increase in the bonding environment as we increase the charge state. Overall, we find that while cationic Ga is capable of defecting into a α-Al_2O_3 crystal thermodynamically, migration of the defect is kinetically prohibited.

ACKNOWLEDGMENTS

G.R.J. would like to acknowledge Drs. Timothy C. Schutt and James M. Christensen for their input on the manuscript and useful discussions. The use of trade, product, or firm names in this report is for descriptive purposes only and does not imply endorsement by the U.S. Government. The tests described and the resulting data presented herein, unless otherwise noted, were obtained from research conducted under the Installation and Operational Environments (IOE) Program of the United States Army Corps of Engineers and the Environmental Security Technology Certification Program of the Department of Defense by the USAERDC (Program Element No. 601102A, Project AB2, Task 03/04). Permission was granted by the Chief of Engineers to publish this information. The findings of this report are not to be construed as an official Department of the Army position unless so designated by other authorized documents. This work was supported by a grant of computer time from the DOD High Performance Computing Modernization Program at ERDC, Vicksburg. This document has been approved for public release (Distribution Statement A). At the time of publication, the IOE Lead Technical Director is Dr. Elizabeth Ferguson, and the IOE 6.1 Basic Research Program Manager is Dr. Tosin Sekoni.

[1] S. K. Das and W. Yin, The worldwide aluminum economy: The current state of the industry, JOM **59**, 57 (2007).
[2] S. T. Mavhungu, E. T. Akinlabi, M. A. Onitiri, and F. M. Varachia, Aluminum matrix composites for industrial use: Advances and trends, Procedia Manufacturing **7**, 178 (2017).
[3] B. Stojanovic, M. Bukvic, and I. Epler, Application of aluminum and aluminum alloys in engineering, App. Eng. Lett. **3**, 52 (2018).
[4] K. Salonitis, M. Jolly, E. Pagone, and M. Papanikolaou, Life-cycle and energy assessment of automotive component manufacturing: The dilemma between aluminum and cast iron, Energies **12**, 2557 (2019).
[5] R. S. Long, E. Boettcher, and D. Crawford, Current and future uses of aluminum in the automotive industry, JOM **69**, 2635 (2017).
[6] M. Bertram, K. J. Martchek, and G. Rombach, Material flow analysis in the aluminum industry, J. Indust. Ecology **13**, 650 (2009).
[7] S. K. Das and J. A. S. Green, Aluminum industry and climate change—assessment and responses, JOM **62**, 27 (2010).
[8] G. Liu, C. E. Bangs, and D. B. Müller, Unearthing potentials for decarbonizing the u.s. aluminum cycle, Environ. Sci. Technol. **45**, 9515 (2011).
[9] J. Safarian and L. Kolbeinsen, Smelting-reduction of bauxite for sustainable alumina production, *2016 Sustainable Industrial Processing Summit and Exhibition*, Vol. 10 (Flogen Star OUTREACH, 2016), p. 149.
[10] A. U. Elinwa and E. Mbadike, The use of aluminum waste for concrete production, J. Asian Arch. Build. Engin. **10**, 217 (2011).
[11] G. Liu and D. B. Müller, Addressing sustainability in the aluminum industry: A critical review of life cycle assessments, J. Cleaner Production **35**, 108 (2012).
[12] E. David and J. Kopac, Aluminum recovery as a product with high added value using aluminum hazardous waste, J. Hazard. Mater. **261**, 316 (2013).
[13] N. Tebbal and Z. E. A. Rahmouni, Valorization of aluminum waste on the mechanical performance of mortar subjected to cycles of freeze-thaw, Proc. Comput. Sci. **158**, 1114 (2019).
[14] A. López-Delgado, J. I. Robla, I. Padilla, S. López-Andrés, and M. Romero, Zero-waste process for the transformation of a hazardous aluminum waste into a raw material to obtain zeolites, J. Cleaner Production **255**, 120178 (2020).
[15] G. Liu, C. Feng, and P. Shao, Degradation of perfluorooctanoic acid with hydrated electron by a heterogeneous catalytic system, Environ. Sci. Technol. c06793 (2021).
[16] A. Shrivastava, M. Krones, and F. E. Pfefferkorn, Comparison of energy consumption and environmental impact of friction stir welding and gas metal arc welding for aluminum, Cirp J. Manufacturing Sci. Technol. **9**, 159 (2015).
[17] M. Köhler, S. Fiebig, J. Hensel, and K. Dilger, Wire and arc additive manufacturing of aluminum components, Metals **9**, 608 (2019).
[18] N. Diaz, E. Redelsheimer, and D. Dornfeld, *Energy Consumption Characterization and Reduction Strategies for Milling Machine Tool Use* (Springer Science and Business Media, Berlin, 2011), pp. 263–267
[19] R. Nur, D. Kurniawan, M. Y. Noordin, and S. Izman, Optimizing power consumption for sustainable dry turning of treated aluminum alloy, Procedia Manufacturing **2**, 558 (2015).
[20] A. Huntington, Embrittlement of brass by mercury, J. Inst. Met. **11**, 108 (1914).
[21] E. Heyn, Internal strains in cold-wrought metals, and some troubles caused thereby, J. Inst. Metals **12**, 1 (1914).
[22] M. H. Kamdar, *Liquid metal embrittlement* (Elsevier, Amsterdam, 1983), pp. 361–459.
[23] Y. Joseph, C. Kuhrs, W. Ranke, M. Ritter, and W. Weiss, Adsorption of water on FeO(111) and Fe_3O_4(111): Identification of active sites for dissociation, Chem. Phys. Lett. **314**, 195 (1999).
[24] D. G. Kolman, A review of recent advances in the understanding of liquid metal embrittlement, Corrosion **75**, 42 (2019).
[25] J. E. Norkett, M. D. Dickey, and V. M. Miller, A review of liquid metal embrittlement: Cracking open the disparate mechanisms, Metall. Mater. Trans. A **52**, 2158 (2021).
[26] A. G. Kalashami, C. DiGiovanni, M. H. Razmpoosh, F. Goodwin, and N. Y. Zhou, The role of internal oxides on the liquid metal embrittlement cracking during resistance spot

welding of the dual phase steel, Metall. Mater. Trans. A **51**, 2180 (2020).

[27] A. R. Westwood and M. H. Kamdar, Concerning liquid metal embrittlement, particularly of zinc monocrystals by mercury, Philos. Mag. **8**, 787 (1963).

[28] C. F. Old and P. Trevena, Liquid metal embrittlement of aluminium single crystals by gallium, Metal Sci. **13**, 591 (1979).

[29] M. H. Kamdar, The occurrence of liquid-metal embrittlement, Physica Status Solidi (a) **4**, 225 (1971).

[30] W. Ludwig and D. Bellet, Penetration of liquid gallium into the grain boundaries of aluminium: a synchrotron radiation microtomographic investigation, Mater. Sci. Eng. **281**, 198 (2000).

[31] R. Tanaka, P.-K. Choi, H. Koizumi, and S. ichi Hyodo, Fast penetration of liquid gallium in polycrystalline aluminum films, Mater. Trans. **42**, 138 (2001).

[32] D. G. Kolman and R. Chavarria, Liquid-metal embrittlement of 7075 aluminum and 4340 steel compact tension specimens by gallium, J. Test. Eval, **30**, 452 (2002).

[33] K. Ina and H. Koizumi, Penetration of liquid metals into solid metals and liquid metal embrittlement, Mater. Sci. Eng.: A **387-389**, 390 (2004).

[34] M. Rajagopalan, M. A. Bhatia, M. A. Tschopp, D. Srolovitz, and K. N. Solanki, Atomic-scale analysis of liquid-gallium embrittlement of aluminum grain boundaries, Acta Mater. **73**, 312 (2014).

[35] M. Shen, Y. Li, C. Hu, S. Xue, C. Xiang, J. Luo, and Z. Yu, The interfacial structure underpinning the al-ga liquid metal embrittlement: Disorder vs. order gradients, Scr. Mater. **204**, 114149 (2021).

[36] F. G. Ferré, M. Ormellese, F. D. Fonzo, and M. G. Beghi, Advanced al_2o_3 coatings for high temperature operation of steels in heavy liquid metals: A preliminary study, Corrosion Sci. **77**, 375 (2013).

[37] A. Yang, C. Ching, M. Easler, D. E. Helbling, and W. R. Dichtel, Cyclodextrin polymers with nitrogen-containing tripodal crosslinkers for efficient pfas adsorption, ACS Mater. Lett. **2**, 1240 (2020).

[38] P. Roy, C. Badie, J. B. Claude, A. Barulin, A. Moreau, J. Lumeau, M. Abbarchi, L. Santinacci, and J. Wenger, Preventing corrosion of aluminum metal with nanometer-thick films of al_2o_3 capped with tio_2 for ultraviolet plasmonics, ACS App. Nano Mater. **4**, 7199 (2021).

[39] C. Wang, S. W. Li, W. H. Fan, Y. C. Zhang, X. Y. Zhang, R. R. Guo, H. J. Lin, S. Y. Lien, and W. Z. Zhu, Structural, optical and morphological evolution of $Ga_2O_3/Al_2O_3(0001)$ films grown at various temperatures by pulsed laser deposition, Ceramics Int. **47**, 29748 (2021).

[40] C. Groot and R. E. Wilson, Intergranular corrosion of aluminum in superheated steam, Ind. Eng. Chem. **49**, 1251 (1957).

[41] F. H. Stott, Y. Shida, D. P. Whittle, G. C. Wood, and B. D. Bastoww, The morphological and structural development ot internal oxides in nickel-aluminum alloys at high temperatures, Oxidation Metals **18**, 127 (1982).

[42] H. J. Grabke and G. H. Meiert, Accelerated oxidation, internal oxidation, intergranular oxidation, and pesting of intermetallic compounds, Oxidation Metals **44**, 147 (1995).

[43] M. I. Grah, K. Alzebdeh, P. Y. Sheng, M. D. Vaudin, K. J. Bowman, and M. Ostoja-starzewskp, Brittle intergranular failure in 2d microstructures: Experiments and computer simulations, Acta. Mater. **44**, 4003 (1996).

[44] V. S. Sinyavskii, V. V. Ulanova, and V. D. Kalinin, On the mechanism of intergranular corrosion of aluminum alloys, Protection Metals **40**, 481 (2004).

[45] M. Navaser and M. Atapour, Effect of friction stir processing on pitting corrosion and intergranular attack of 7075 aluminum alloy, J. Mater. Sci. Technol. **33**, 155 (2017).

[46] M. L. de Bonfils-Lahovary, L. Laffont, and C. Blanc, Characterization of intergranular corrosion defects in a 2024 T351 aluminium alloy, Corrosion Sci. **119**, 60 (2017).

[47] Y. Yang, A. Kushima, W. Han, H. Xin, and J. Li, Liquid-like, self-healing aluminum oxide during deformation at room temperature, Nano Lett. **18**, 2492 (2018).

[48] S. Kumari, S. Wenner, J. C. Walmsley, O. Lunder, and K. Nisancioglu, Progress in understanding initiation of intergranular corrosion on AA6005 aluminum alloy with low copper content, J. Electrochem. Soc. **166**, C3114 (2019).

[49] C.-F. Lin, K.-S. Chang, C.-W. Tsay, D.-Y. Lee, S.-L. Lo, and T. Yasunaga, Adsorption Mechanism of Gallium(Iii) and Indium(Iii) Onto γ-Al_2O_3, J. Colloid Inter. Sci. **188**, 201 (1997).

[50] K. Motoki, Development of gallium nitride substrates, Sei Tech. Rev. **70**, 28 (2010).

[51] H. J. Quah and K. Y. Cheong, Surface passivation of gallium nitride by ultrathin rf-magnetron sputtered Al_2O_3 gate, ACS App. Mater. Inter. **5**, 6860 (2013).

[52] A. B. Serban, V. L. Ene, C. C. Gheorghiu, D. Balabanski, E. Andronescu, and V. Leca, Rf magnetron sputtering of gallium nitride (gan) on sapphire substrate, Bull., Series B **81**, 11 (2019).

[53] Y. Yang, R. Fan, P. Zhang, L. Wang, M. Pan, Q. Wang, X. Xie, S. Xu, C. Wang, C. Wu, M. Xu, J. Jin, and D. W. Zhang, In situ h-radical surface treatment on aluminum gallium nitride for high-performance aluminum gallium nitride/gallium nitride mis-hemts fabrication, Micromachines **14**, 1278 (2023).

[54] Y. An, L. Dai, Y. Wu, B. Wu, Y. Zhao, T. Liu, H. Hao, Z. Li, G. Niu, J. Zhang, Z. Quan, and S. Ding, Epitaxial growth of β-Ga_2O_3 thin films on Ga_2O_3 and Al_2O_3 substrates by using pulsed laser deposition, J. Adv. Dielect. **09**, 1950032 (2019).

[55] J. N. D. de Leon, A. Cruz-Taboada, Y. Esqueda-Barron, G. Alonso-Nuñez, S. Loera-Serna, A. M. Venezia, M. E. Poisot, and S. Fuentes-Moyado, Catalytic dehydration of 2-propanol over Al_2O_3-Ga_2O_3 and Pd/Al_2O_3-Ga_2O_3 catalysts, Catal. Today **356**, 339 (2020).

[56] E. Puello-Polo, Y. Pájaro, and E. Márquez, Effect of the gallium and vanadium on the dibenzothiophene hydrodesulfurization and naphthalene hydrogenation activities using sulfided NiMo-V_2O_5/Al_2O_3-Ga_2O_3, Catalysts **10**, 894 (2020).

[57] E. Puello-Polo, N. R. Checca-Huaman, E. O. López, C. A. Toloza, and F. J. Méndez, Adsorptive desulfurization properties of refractory sulfur compounds onto Al_2O_3-Ga_2O_3 nanomaterials, Ceramics Int. **49**, 27622 (2023).

[58] R. Yang and A. P. Rendell, First principles study of gallium atom adsorption on the α-$Al_2O_3(0001)$ surface, J. Phys. Chem. B **110**, 9608 (2006).

[59] J. Enkovaara, C. Rostgaard, J. J. Mortensen, J. Chen, M. Dułak, L. Ferrighi, J. Gavnholt, C. Glinsvad, V. Haikola, H. a Hansen, H. H. Kristoffersen, M. Kuisma, a H Larsen, L.

Lehtovaara, M. Ljungberg, O. Lopez-Acevedo, P. G. Moses, J. Ojanen, T. Olsen, V. Petzold *et al.*, Electronic structure calculations with gpaw: A real-space implementation of the projector augmented-wave method, J. Phys.: Condens. Matter **22**, 253202 (2010).

[60] A. H. Larsen, J. J. Mortensen, J. Blomqvist, I. E. Castelli, R. Christensen, M. Dułak, J. Friis, M. N. Groves, B. Hammer, C. Hargus, E. D. Hermes, P. C. Jennings, P. B. Jensen, J. Kermode, J. R. Kitchin, E. L. Kolsbjerg, J. Kubal, K. Kaasbjerg, S. Lysgaard, J. B. Maronsson *et al.*, The atomic simulation environment—a python library for working with atoms, J. Phys.: Condens. Matter **29**, 273002 (2017).

[61] J. J. Mortensen, L. B. Hansen, and K. W. Jacobsen, Real-space grid implementation of the projector augmented wave method, Phys. Rev. B **71**, 035109 (2005).

[62] P. E. Blöchl, Projector augmented-wave method, Phys. Rev. B **50**, 17953 (1994).

[63] G. Kresse and D. Joubert, From ultrasoft pseudopotentials to the projector augmented-wave method, Phys. Rev. B **59**, 1758 (1999).

[64] E. L. Briggs, D. J. Sullivan, and J. Bernholc, Real-space multigrid-based approach to large-scale electronic structure calculations, Phys. Rev. B **54**, 14362 (1996).

[65] P. Pulay, Convergence acceleration of iterative sequences. the case of scf iteration, Chem. Phys. Lett. **73**, 393 (1980).

[66] D. M. Wood and A. Zunger, A new method for diagonalising large matrices, J. Phys. A: Math. Gen. **18**, 1343 (1985).

[67] S. B. Zhang and J. E. Northrup, Chemical potential dependence of defect formation energies in gaas: Application to ga self-diffusion, Phys. Rev. Lett. **67**, 2339 (1991).

[68] C. G. V. de Walle, First-principles calculations for defects and impurities: Applications to iii-nitrides, J. App. Phys. **95**, 3851 (2004).

[69] E. G. Seebauer and M. C. Kratzer, Charged point defects in semiconductors, Mater. Sci. Eng. R: Rep. **55**, 57 (2006).

[70] C. Freysoldt, J. Neugebauer, and C. G. Van de Walle, Fully ab initio finite-size corrections for charged-defect supercell calculations, Phys. Rev. Lett. **102**, 016402 (2009).

[71] H.-P. Komsa and A. Pasquarello, Finite-size supercell correction for charged defects at surfaces and interfaces, Phys. Rev. Lett. **110**, 095505 (2013).

[72] R. Bader, *Atoms in Molecules: A Quantum Theory* (Clarendon, Oxford, 1994).

[73] G. Henkelman, A. Arnaldsson, and H. Jónsson, A fast and robust algorithm for bader decomposition of charge density, Comput. Mater. Sci. **36**, 354 (2006).

[74] E. Sanville, S. D. Kenny, R. Smith, and G. Henkelman, Improved grid-based algorithm for bader charge allocation., J. Comput. Chem. **28**, 899 (2007).

[75] W. Tang, E. Sanville, and G. Henkelman, A grid-based bader analysis algorithm without lattice bias., J. Phys.: Condens. Matter **21**, 084204 (2009).

[76] G. Henkelman and H. Jónsson, Improved tangent estimate in the nudged elastic band method for finding minimum energy paths and saddle points, J. Chem. Phys. **113**, 9978 (2000).

[77] D. A. McQuarrie, *Statistical Mechanics* (Harper & Row, New York, 1975).

[78] C. S. Barrett and F. J. Spooner, Lattice constants of gallium at 297 ° K, Nature (London) **207**, 1382 (1965).

[79] A. S. Cooper, Precise lattice constants of germanium, aluminum, gallium arsenide, uranium, sulphur, quartz and sapphire, Acta Cryst **15**, 578 (1962).

[80] J. Lewis, D. Schwarzenbach, and H. D. Flack, Electric field gradients and charge density in corundum, α-Al_2O_3, Acta Cryst. A **38**, 733 (1982).

[81] G. V. G. V. Samsonov, *The Oxide Handbook* (IFI/Plenum, New York, 1973).

[82] W. Y. Ching and Y.-N. N. Xu, First-principles calculation of electronic, optical, and structural properties of α-Al_2O_3, J. Am. Ceram. Soc. **77**, 404 (1994).

[83] T. V. Perevalov, A. V. Shaposhnikov, V. A. Gritsenko, H. Wong, J. H. Han, and C. W. Kim, Electronic structure of α-Al_2O_3: Ab initio simulations and comparison with experiment, JETP Lett. **85**, 165 (2007).

[84] S. Riaz, S. Shamaila, B. Khan, and S. Naseem, Lower temperature formation of alumina thin films through sol-gel route, Surf. Rev. Lett. **15**, 681 (2008).

[85] J. M. McHale, Surface energies and thermodynamic phase stability in nanocrystalline aluminas, Science **277**, 788 (1997).

[86] G. Busca, *Structural, Surface, and Catalytic Properties of Aluminas*, 1st ed. (Elsevier, Amsterdam, 2014), pp. 319–404.

[87] G. R. Jenness and D. G. Vlachos, Dft study of the conversion of furfuryl alcohol to 2-methylfuran on RuO_2 (110), J. Phys. Chem. C **119**, 5938 (2015).

[88] G. R. Jenness, J. Seiter, and M. K. Shukla, Dft investigation on the adsorption of munition compounds on α-Fe_2O_3: Similarity and differences with α-Al_2O_3, Phys. Chem. Chem. Phys. **20**, 18850 (2018).

[89] G. R. Jenness, S. A. Giles, and M. K. Shukla, Thermodynamic adsorption states of tnt and dnan on corundum and hematite, J. Phys. Chem. C **124**, 13837 (2020).

[90] G. R. Jenness and M. K. Shukla, Effect of concrete composition on the thermodynamic binding of dopamine: A dft study, Langmuir **38**, 472 (2022).

[91] W. A. Pisani, G. R. Jenness, T. C. Schutt, S. L. Larson, and M. K. Shukla, Preferential adsorption of prominent amino acids in the urease enzyme of *sporosarcina pasteurii* on arid soil components: A periodic dft study, Langmuir **38**, 13414 (2022).

[92] J. P. Perdew and Y. Wang, Accurate and simple analytic representation of the electron-gas correlation energy, Phys. Rev. B **45**, 13244 (1992).

[93] J. P. Perdew, K. Burke, and M. Ernzerhof, Generalized gradient approximation made simple, Phys. Rev. Lett. **77**, 3865 (1996).

[94] J. Klimeš, D. R. Bowler, and A. Michaelides, Chemical accuracy for the van der waals density functional, J. Phys.: Condens. Matter **22**, 022201 (2010).

[95] J. Klimeš, D. R. Bowler, and A. Michaelides, Van der waals density functionals applied to solids, Phys. Rev. B **83**, 195131 (2011).

[96] J. P. Perdew, A. Ruzsinszky, G. I. Csonka, O. A. Vydrov, G. E. Scuseria, L. A. Constantin, X. Zhou, and K. Burke, Restoring the density-gradient expansion for exchange in solids and surfaces, Phys. Rev. Lett. **100**, 136406 (2008).

[97] See Supplemental Material at http://link.aps.org/supplemental/10.1103/PhysRevB.109.235204 for plots of the chemical potentials of Ga, Al, and α-Al_2O_3 versus k-point density, tables of atomic charges, volumes, and bonds for Ga nearest

neighbors, and figures of charge density differences for Wyckoff sites 6b, 18d, and 36f.

[98] M. I. Aroyo, J. M. Perez-Mato, C. Capillas, E. Kroumova, S. Ivantchev, G. Madariaga, A. Kirov, and H. Wondratschek, Bilbao crystallographic server: I. databases and crystallographic computing programs, Z. Kristallogr. **221**, 15 (2006).

[99] R. M. Jacobs, J. H. Booske, and D. Morgan, Intrinsic defects and conduction characteristics of Sc_2O_3 in thermionic cathode systems, Phys. Rev. B **86**, 054106 (2012).

[100] J.-P. Crocombette, D. Torumba, and A. Chartier, Charge states of point defects in uranium oxide calculated with a local hybrid functional for correlated electrons, Phys. Rev. B **83**, 184107 (2011).

[101] J. Ma, S. H. Wei, T. A. Gessert, and K. K. Chin, Carrier density and compensation in semiconductors with multiple dopants and multiple transition energy levels: Case of cu impurities in cdte, Phys. Rev. B **83**, 245207 (2011).

[102] https://www.cryst.ehu.es/cgi-bin/cryst/programs/nph-wp-list.